

Effect of Hydration on Promoting Oxidative Reactions with Aluminum Oxide and Oxyhydroxide Nanoparticles

I. Shancita,[†] Loudon Lee Campbell,[†] Chi-Chin Wu,^{*,‡} Adelia J. A. Aquino,^{*,||,⊥} Scott D. Walck,[§] Daniel Tunega,^{*,⊥} and Michelle L. Pantoya^{*,†,||}

[†]Department of Mechanical Engineering, Texas Tech University, Lubbock, Texas 79409, United States

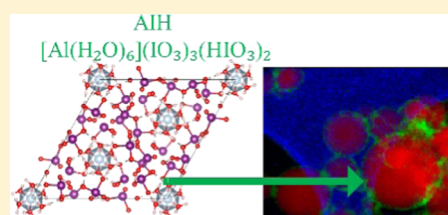
[‡]Lethality Division, Weapons and Materials Research Directorate and [§]Survive Engineering Co., U.S. Army Research Laboratory, Aberdeen Proving Ground, Aberdeen, Maryland 21005, United States

^{||}Department of Chemistry and Biochemistry, Texas Tech University, Lubbock, Texas 79409-1061, United States

[⊥]Institute for Soil Research, University of Natural Resources and Life Sciences, Peter-Jordan-Strasse 82, Wien A-1190, Austria

Supporting Information

ABSTRACT: To harness greater power from aluminum (Al) combustion, one approach is to chemically transform the aluminum oxide (Al_2O_3) passivation layer surrounding the Al core particle by exploiting surface reactions via a wet chemistry approach. The goal of this study is to identify key parameters affecting interfacial chemistry on Al particles. As models for the surface layer of Al particles, γ aluminum oxide ($\gamma\text{-Al}_2\text{O}_3$) and boehmite ($\gamma\text{-AlO}(\text{OH})$) nanoparticles are examined. Density functional theory calculations of dehydroxylation and dehydration energies are conducted on $\gamma\text{-Al}_2\text{O}_3$ and $\gamma\text{-AlO}(\text{OH})$. The calculations predict that OH bridge bonds throughout $\gamma\text{-AlO}(\text{OH})$ require similar energy to break compared with terminal OH groups abundant on the surface of $\gamma\text{-Al}_2\text{O}_3$ and are the most reactive sites. Experimentally, the predictions are confirmed by isolating representative surface reactions using $\gamma\text{-Al}_2\text{O}_3$ and $\gamma\text{-AlO}(\text{OH})$ nanoparticles suspended in an iodic acid solution to synthesize an oxidizing salt, aluminum iodate hexahydrate (AIH). Powder X-ray diffraction and X-ray photoelectron spectroscopy identify species of whole materials and surfaces, respectively. The structural and compositional details are revealed by acquiring images, spectra, and determining component phase maps in the scanning mode via transmission electron microscopy. The AIH yield is higher for $\gamma\text{-Al}_2\text{O}_3$, AIH formation is linked to the removal of terminal OH bonds, and AIH appears isolated on the particle surface. AIH formation from $\gamma\text{-AlO}(\text{OH})$ is linked to the removal of OH bridge bonds, and AIH formation does not appear localized on particle surfaces. These results link dehydroxylation and dehydration energies to reactions that produce AIH and provide a fundamental understanding of how to use hydration to control Al_2O_3 surface reactions and transform the reactivity of Al particles. Also, AIH is newly discovered as a highly reactive oxidizer used in energetic material studies that show tremendous potential for increasing the energy release rate from Al combustion.



1. INTRODUCTION

Aluminum (Al) powder is used as a fuel for many energetic material applications. The Al particles are passivated with a thin (i.e., 4–5 nm thick) layer of amorphous aluminum oxide (Al_2O_3) that acts as a barrier to the diffusion oxidation reaction with the Al core. During combustion, Al_2O_3 also acts as a heat sink inhibiting energy transfer. The influence of the Al_2O_3 shell on Al particle reactivity is especially apparent for nano-aluminum (nAl) particles that have a higher surface area to volume ratio and, therefore, a greater concentration of Al_2O_3 than micron Al particles. For example, the Al_2O_3 passivation shell can promote nAl combustion through a melt dispersion mechanism when heating rates are in excess of 10^6 K/s^{1,2} or can retard combustion in slower heating rate formulations because of the abundance of Al_2O_3 ³ acting as a heat sink.

To enhance Al reactivity, many researchers examined alternative passivation materials surrounding nAl particles. Chemical functionalization of the particle surface is one approach.^{4–6} For example, Crouse et al.⁷ used three different

acrylic monomers functionalized on the nAl surface to reduce agglomerations and facilitate compatibility between the nAl particles in various aqueous suspensions. Further studies showed that nAl particle energy release rate was enhanced due to the lower decomposition temperature of the polymeric passivation that reacted with both the shell (Al_2O_3) and core (Al) of the particles.⁸ Ultimately, these researchers introduced a new approach to harness greater power from metal fuel particles by exploring different fuel particle passivation materials that offer tailorable properties.

More recently, the Al_2O_3 shell on nAl was replaced by an oxidizing salt called aluminum iodate hexahydrate [$\text{Al}(\text{H}_2\text{O})_6](\text{IO}_3)_3(\text{H}_2\text{O})_2$, AIH].^{9,10} The resulting reactivity of AIH-coated nAl (AIH–nAl) particles was astounding. Gottfried et al.¹⁰ showed that AIH–nAl particles have the

Received: March 20, 2019

Revised: May 18, 2019

Published: June 10, 2019

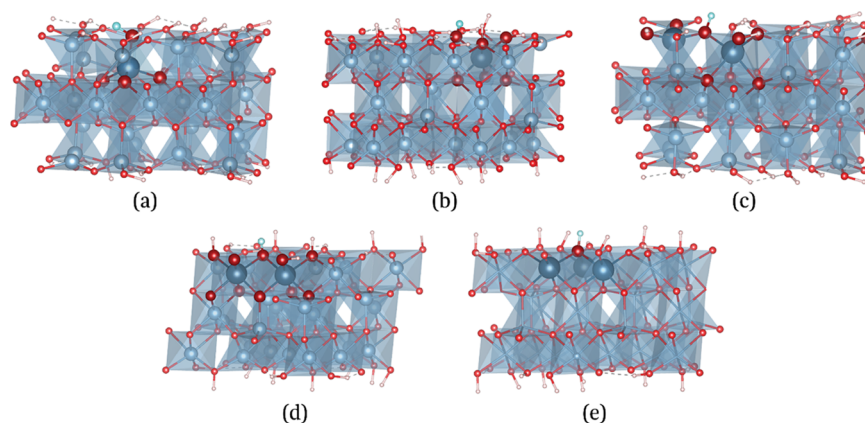


Figure 1. Periodic slab models of OH sites for (111) surfaces of γ - Al_2O_3 : (a) Ia ($\text{Al}_{\text{IV}}\text{-OH}$); (b) Ib ($\text{Al}_{\text{VI}}\text{-OH}$); (c) IIa (bridged $\text{Al}_{\text{IV}}\text{-OH-Al}_{\text{VI}}$); (d) IIb (bridged $\text{Al}_{\text{VI}}\text{-OH-Al}_{\text{VI}}$); and, (e) III OH bound to 3 Al_{VI} . Hydrogen atoms are displayed as white spheres, oxygen atoms are displayed as red spheres, and aluminum atoms are displayed as polyhedral blue. The specific sites of dehydroxylation are emphasized: H is displayed as a cyan sphere, O atoms are displayed as large dark red spheres, and Al atoms are displayed as large blue spheres. Computational cell vectors are omitted for clarity.

potential to react at time scales relevant to a detonation event. A metallic particle that can be optimized to contribute more energy to a detonation event is an important improvement in particle combustion. Metal particles normally react by mass diffusion mechanisms that limit the energy release rate to deflagrations. The potential applications for AIH- $n\text{Al}$ particles in detonations motivate further investigation in the hope of producing a new energy source for power generation.

The oxidizing salt, AIH, can be synthesized by suspending $n\text{Al}$ particles in a liquid iodic acid (HIO_3) solution.^{9,11,12} However, the process does not produce repeatable concentrations of AIH on $n\text{Al}$ particles. For example, one sample produced 6 wt % AIH on $n\text{Al}$,¹⁰ another produced 15 wt % AIH on $n\text{Al}$,¹⁰ whereas 80 wt % AIH on $n\text{Al}$ was produced in Smith et al.^{9,12} A reaction scheme was proposed to explain the replacement of Al_2O_3 by AIH through a polarization mechanism,^{9,12} which is a function of solution pH and electrostatic forces between H_3O^+ in solution and Al-O bonds in the Al_2O_3 passivation layer on $n\text{Al}$ particles. By polarizing the Al-O bond in Al_2O_3 , H_2O is formed from oxygen in Al_2O_3 and H_3O^+ that produce $[\text{Al}(\text{H}_2\text{O})_6]^{3+}$. Then, the formation of AIH is dependent on the concentration of $[\text{Al}(\text{H}_2\text{O})_6]^{3+}$ available, which is associated with water molecules in the solution. It is also noted that pure AIH has also been produced from a similar wet chemistry approach but with various starting materials. For example, Cradwick et al.¹³ synthesized AIH from an anion salt $\text{Al}[\text{IO}_3]_2[\text{NO}_3] \cdot 6\text{H}_2\text{O}$, prepared by mixing Al particles with iodic acid solution. After removing the nitrate salt, AIH was crystallized as the acid salt $\text{Al}[\text{IO}_3]_3 \cdot 2\text{HIO}_3 \cdot 6\text{H}_2\text{O}$. Also, Kidyarov et al.¹⁴ dissolved aluminum hydroxides, $\text{Al}(\text{OH})_3$, in iodic acid to form pure aluminum iodate octahydrate ($\text{Al}(\text{IO}_3)_3 \cdot 8\text{H}_2\text{O}$).

The goal of this study is to examine surface reactions associated with Al particles and iodic acid that promote the formation of AIH. This goal is accomplished by isolating reactions between iodic acid and Al-O structured materials including γ - Al_2O_3 and γ - $\text{AlO}(\text{OH})$ nanoparticles, representative of the Al particle surface. The core (Al)-shell (Al_2O_3) structure inherent with Al particles demands the investigation of Al_2O_3 , and the natural hydration associated with Al_2O_3 also spurs questions regarding the influence of hydration on reactivity. The objective is to model hydroxyl bonding on γ -

Al_2O_3 and γ - $\text{AlO}(\text{OH})$ using density functional theory (DFT) to predict the dehydroxylation and dehydration energies that facilitate reaction pathways favoring AIH formation. A second objective is to experimentally synthesize AIH from γ - Al_2O_3 and γ - $\text{AlO}(\text{OH})$ suspended in iodic acid and confirm DFT-calculated predictions using surface characterization techniques. Specifically, transmission electron microscopy (TEM) and X-ray photoelectronic spectroscopy (XPS) are used to identify the morphology and chemical species as well as surface hydroxyl removal and AIH formation, respectively.

2. METHODS

2.1. Density Functional Theory Calculations. All calculations with periodic boundary conditions were performed using the Vienna ab initio simulation package (VASP),^{15,16} a program code based on Kohn-Sham electron density functional theory (DFT). In the calculations, exchange-correlation energy was expressed in the frame of the generalized gradient approximation (GGA) using the Perdew-Burke-Ernzerhof (PBE) functional.¹⁷ The electron-ion interactions were described by atomic pseudopotentials and the projector-augmented-wave (PAW) method^{18,19} in a plane-wave basis set with an energy cutoff of 600 eV. The relaxation criteria were 10^{-5} eV for the total electronic energy change and 10^{-4} eV/Å for the maximal allowed forces acting on each atom. Dispersion corrections were included in the calculations using the Grimme D3 scheme.²⁰ Since all computational cells are large enough, Brillouin-zone sampling was restricted to the Γ -point. No symmetry restrictions were applied during the relaxation procedure.

The cluster calculations were also performed at the DFT level of theory using the Becke, three-parameter, Lee-Yang-Parr (B3-LYP) functional²¹ and the split valence polarization (SVP) basis set²² approach with the Turbomole program suite.²³ The calculations were carried out for isolated clusters in vacuum and for clusters immersed in a polar environment represented by water at 298.15 K with a relative permittivity, ϵ , of 78.54.²⁴ Adding the effect of a polar environment on dehydroxylation reactions provides insight into how reactive sites are affected in the iodic acid, a highly polar medium. For the latter, the conductor-like screening model (COSMO) method²⁴ was used. In the geometry optimization procedure,

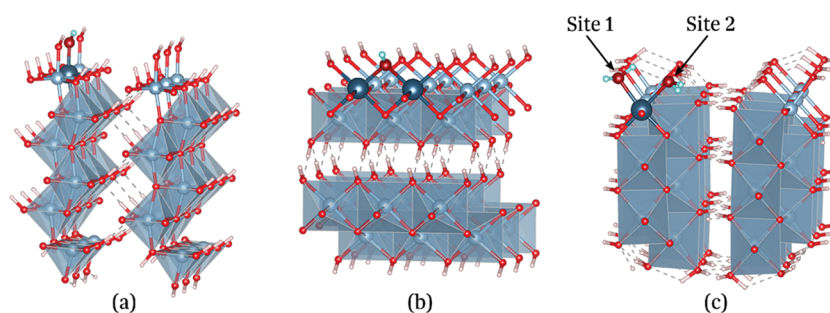


Figure 2. Periodic slab models of OH/H₂O sites for typical surface planes of boehmite: (a) terminal OH at (001) surface, (b) bridged OH at (010) surface, and (c) two H₂O sites at (100) surface. Hydrogen atoms are displayed as white spheres, oxygen atoms are displayed as red spheres, and aluminum atoms are displayed as polyhedral blue. The specific sites of dehydroxylation/dehydration are emphasized: H is displayed as a cyan sphere, O atoms are displayed as large dark red spheres, and Al atoms are displayed as large blue spheres. Computational cell vectors are omitted for clarity.

only selected aluminum, oxygen, and hydrogen atoms at the –OH surface could relax, maintaining the rest of the system frozen to preserve the structural environment. The D3 dispersion correction²⁰ was included in the cluster calculations to model the dispersion interactions. The cluster computations were carried out for dehydroxylation reactions at the γ -Al₂O₃ surface.

The surface slab and cluster models of γ -Al₂O₃ and the slab models of γ -AlO(OH) were constructed from known experimental bulk structures by slicing them along defined crystallographic planes. For γ -Al₂O₃, the ideal (not defective) bulk structure determined by single-crystal X-ray diffraction²⁵ was used. Three slab models were created by adding protons to surface O atoms to obtain all known surface OH sites (i.e., Ia, IIa, Ib, IIb, and III according to Knözinger and Ratnasamy²⁶). The cluster models were constructed from the slab models, details can be found in Padhye et al.²⁷ Sites Ia and Ib are terminal OH groups linked to four- and six-coordinated Al (Al_{IV}–OH and Al_{VI}–OH), sites IIa and IIb are bridged OH groups (Al_{IV}–OH–Al_{VI} and Al_{VI}–OH–Al_{VI}), and site III represents OH group bound to 3 Al_{VI} atoms. Figure 1 displays all 5 periodic slab models of the (111) surfaces of γ -Al₂O₃ (stoichiometry formulas and computational cell vectors are given in the Supporting Information, Table S1).

For creating periodic surface models of γ -AlO(OH), the initial bulk structure, including the position of H atoms, was taken from Noel et al.²⁸ The slab models represent the three most abundant crystallographic lowest-index surfaces: (100), (010), and (001) (Figure 2). Miller indexing is that of the A2₁am space group. The surface (010) has a natural termination by bridged OH groups as γ -AlO(OH) was a layered material with layers terminated by OH groups and layer stacking along the *b* vector. The layers were joined together by hydrogen bonding. In the case of the other two surfaces, the under-coordinated surface Al atoms were saturated by water molecules on the (100) surface and by terminal hydroxyl groups on the (001) surface, in accord with the previous modeling of γ -AlO(OH).²⁹ Stoichiometry formulas and computational cell vectors of all three models are given in the Supporting Information, Table S1.

The surface coating was simulated such that all slab models were neutral. In this way, the OH coating was 100% for γ -AlO(OH) and 60% for γ -Al₂O₃. The thickness of the slabs was about 8 Å (γ -Al₂O₃) or 11–12 Å (γ -AlO(OH)). In all models, a vacuum space with a thickness of about 20 Å was imposed above the slab surface to minimize interactions between

periodic images. The lateral computational cell vectors were optimized, and their dimensions were at least 8.7 Å.

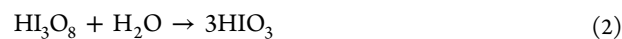
The dehydroxylation calculations were performed by removing a particular OH group from the surface, creating unsaturated Al atom(s) at the surface and optimizing all positions of the slab cation (+1), keeping the cell parameters fixed. The isolated OH anion was always optimized in the same unit cell as the corresponding original slab. The dehydration energies for the (100) surface of boehmite were calculated by removing one water molecule from the surface. In this case, no charged systems were involved. Dehydroxylation and dehydration energies $\Delta E_{\text{dhx}}/\Delta E_{\text{dhy}}$ for the γ -AlO(OH) slab were calculated according to eq 1a. In this equation, E_{slab} is the total electronic energy of the optimized neutral slab, and $E_{\text{ssc}^+/\text{ssc}}$ is the total electronic energy of the optimized surface slab cation (dehydroxylation) and the neutral slab (dehydration); $E_{\text{OH}^-/\text{H}_2\text{O}}$ is the total energy of the isolated hydroxyl anion and the water molecule, respectively. Equation 1a was also used to calculate the dehydroxylation energy of the γ -Al₂O₃ slab. An analogous procedure was followed in the cluster calculations (eq 1b) for the γ -Al₂O₃ clusters, where E_{cl^+} and E_{cl} are total electronic energies of positively charged and neutral clusters, respectively.

$$\Delta E_{\text{dhx/dhy}} = (E_{\text{ssc}^+/\text{ssc}} + E_{\text{OH}^-/\text{H}_2\text{O}}) - E_{\text{slab}} \quad (1a)$$

$$\Delta E_{\text{dhx}} = (E_{\text{cl}^+} + E_{\text{OH}^-}) - E_{\text{cl}} \quad (1b)$$

It should be noted that charged systems represent a problem for periodic calculations. Thus, the absolute dehydroxylation energy values may not be accurate but are comparable between each other if the same vacuum is used in each model. The problem with the charged systems does not appear in the calculations on the cluster models. The calculated dehydroxylation energies should be more accurate even though long-range (electrostatic) interactions are missing in the cluster calculations.

2.2. Materials. Powder HI₃O₈ (Sigma Aldrich, St. Louis, MO) was dissolved in distilled water in 2:1 (i.e., powder/water) mass ratio to produce a solution of aqueous iodic acid (HIO₃), according to the following reaction.³⁰



A magnetic stirrer mixed the solution in a beaker for about 20 min at 360 rpm to produce a clear liquid solution known to be highly acidic with a pH value <0.2.⁹ The solid precipitate from the solution was reclaimed after liquid evaporation under

ambient conditions followed by powder X-ray diffraction (PXRD) analyses. The solid precipitate was 70 wt % HIO_3 , 23 wt % HI_3O_8 , and 7 wt % amorphous material and confirms partial recrystallization of HI_3O_8 .

The precursor materials were $\gamma\text{-Al}_2\text{O}_3$ and $\gamma\text{-AlO(OH)}$ nanopowders supplied by Sigma Aldrich (St. Louis, MO) and US Research Nanomaterials Inc. (Houston, TX), respectively. Table 1 shows physical property data from TEM and PXRD

Table 1. Specific Surface Area (BET) and TEM Evaluated Particle Size for Starting Materials

materials	specific surface area (SSA) (m^2/g)	particle size (nm) observed from TEM	particle morphology
$\gamma\text{-Al}_2\text{O}_3$	121	length: 5–52 nm thickness: 4–7 nm	rod like
$\gamma\text{-AlO(OH)}$	229	length: 7–39 nm thickness: 2–9 nm	rod like

analysis. Figure S1 in the Supporting Information shows TEM images as well as PXRD scans for each precursor material. Also, specific surface area (SSA) measurements were performed using a multipoint Brunauer–Emmett–Teller (BET) method in a Quantachrome autosorb iQ instrument (Boynton Beach, FL).

2.3. Synthesis Method. The pH of the aqueous solution was constant based on the mass ratio of HI_3O_8 to H_2O (2:1) to form iodic acid (HIO_3) in all experiments. The $\gamma\text{-Al}_2\text{O}_3$ to HIO_3 ratio was fixed at a 1:6 molar ratio of $\text{Al}_2\text{O}_3/\text{HIO}_3$, and the $\gamma\text{-AlO(OH)}$ to HIO_3 ratio was fixed at a 1:10 molar ratio of $\text{AlO(OH)}/\text{HIO}_3$. However, because the final Al/HIO_3 molar ratios are not the same, i.e., 1:3 and 1:10 for $\gamma\text{-Al}_2\text{O}_3$ and $\gamma\text{-AlO(OH)}$, respectively, the resultant Al ion concentrations are different in each iodic acid mixture. This may cause slight differences in the acidity of the final solutions, which in turn might exert a secondary influence on the resulting formation of AIH. Both Al species are weakly soluble, and their solubility strongly depends on pH. Comparing solubility curves as a function of pH (Figure 1 in ref 31 for $\gamma\text{-AlO(OH)}$ and Figure 7 in 32 for $\gamma\text{-Al}_2\text{O}_3$), we can suppose that dissolution kinetics of both species in strongly acidic solution will differ, and, consequently, Al^{3+} concentrations and pH will differ as well. These factors may influence AIH formation.

Each solution was spatula-mixed for 5 min with a 2 g overall mass. The mixtures were dried in an oven at an elevated temperature of 60 °C for 24 h. The dried samples were

reclaimed, and the concentration of crystalline AIH was measured by PXRD. The procedure was repeated five times for each precursor and a sample with a constant 11 wt % AIH concentration derived from each precursor material was further analyzed using XPS and TEM and identified as $\gamma\text{-Al}_2\text{O}_3/\text{AIH}$ or $\gamma\text{-AlO(OH)}/\text{AIH}$ (i.e., indicating the precursor material and constant 11 wt % AIH concentration in the product material).

2.4. Powder X-ray Diffraction (PXRD). Powder XRD was performed using a Rigaku Ultima III powder diffractometer. Data were collected from 15 to 60° 2θ with parallel beam geometry in continuous θ – 2θ mode and data collection time was 2°/min with a step size of 0.02° and analyzed using the MDI Jade V9.1.1 software both for quantitative and qualitative analyses.

2.5. Transmission Electron Microscopy (TEM). The TEM specimens were prepared via the nanoparticle suspension technique by dispersing the sample powders in acetonitrile on the holey carbon film-coated TEM specimen supporting grids (Ted Pella, Inc.). The samples were studied using a JEOL 2100FX TEM operated at 200 keV (JEOL USA, Inc.) The samples were imaged using bright field (BF) conditions and collected using a Gatan Digital Micrograph and an Orius digital camera (Gatan, Inc). Selected area diffraction (SAD) patterns were acquired using a nominal 25 cm camera length with the Gatan formatted images imported and analyzed using the software CSpot (CrystOrient Inc.) with the actual, calibrated camera length for the microscope. The chemical analyses were performed by acquiring X-ray energy-dispersive spectra (XEDS) using an Octane Elite T windowless detector with the TEAM Analysis software (EDAX Inc). Elemental X-ray maps were derived from spectrum images acquired with the EDAX system in the scanning transmission electron microscopy (STEM) mode and postprocessed using the Multivariate Statistical Analysis (MSA) technique with the Automated eXpert Spectral Image Analysis (AXSIA) multivariate toolbox.^{33,34}

2.6. X-ray Photoelectron Spectroscopy (XPS). X-ray photoelectron spectroscopy (XPS) was performed using an Al $K\alpha$ source with a PHI 5000 Versa Probe. For curve fitting evaluation, all peaks were shifted according to the referenced value of C–C bond of C 1s photo peak at 284.8 eV. A Shirley background was used for the background correction for all spectra. Curve fitting of high-resolution spectra was carried out by deconvolution of the peaks engaging Gaussians and Lorentzians models using the Multipak software.

Table 2. Dehydroxylation/Dehydration Energies for Typical Surface OH/ H_2O Sites of $\gamma\text{-Al}_2\text{O}_3$ and $\gamma\text{-AlO(OH)}$ Calculated Using DFT(PBE/D3) and Periodic Surface Slab Models

	OH site	Al-binding		ΔE_{deh} (kJ/mol)	figure
$\gamma\text{-Al}_2\text{O}_3$	Ia	$\text{Al}_{\text{IV}}\text{-OH}$		231.8	1a
	Ib	$\text{Al}_{\text{VI}}\text{-OH}$		163.2	1b
	IIa	$\text{Al}_{\text{IV}}\text{-OH-Al}_{\text{VI}}$		318.0	1c
	IIb	$\text{Al}_{\text{VI}}\text{-OH-Al}_{\text{VI}}$		314.2	1d
	III	$3\text{Al}_{\text{VI}}\text{-OH}$		418.0	1e
$\gamma\text{-AlO(OH)}$	OH site	Al-binding	plane	ΔE_{deh} (kJ/mol)	figure
	terminal	Al–OH	(001)	313.0	2a
	bridge	Al–OH–Al–	(010)	240.6	2b
$\gamma\text{-AlO(OH)}$	H_2O site	Al-binding	plane	ΔE_{deh} (kJ/mol)	figure
	terminal 1	Al–OH ₂	(100)	80.8	2c
	terminal 2	Al–OH ₂	(100)	124.3	2c

3. RESULTS AND DISCUSSION

3.1. DFT Calculations. The dehydroxylation and dehydration energies for the periodic slab models calculated according to eq 1a are collected in Table 2 as a function of the OH coordination shown in Figures 1 and 2. The influence of the polar environment using the cluster models is shown in Table 3. The trends in dehydroxylation energy for γ -Al₂O₃ are

Table 3. Dehydroxylation Energies for Typical Surface OH Sites of γ -Al₂O₃ Using Cluster Models and the B3-LYP/D3/SVP Approach^a

	OH site	Al-binding	ΔE_{deh} (kJ/mol)		
			isolated	polar medium	reduction
γ -Al ₂ O ₃	Ia	Al _{IV} -OH	1003.0	539.3	46%
	Ib	Al _{VI} -OH	924.7	462.0	50%
	IIa	Al _{IV} -OH-Al _{VI}	1109.2	550.6	50%
	IIb	Al _{VI} -OH-Al _{VI}	1249.0	733.9	41%
	III	3 Al _{VI} -OH	1441.0	899.1	40%

^aThe reduction in dehydroxylation energy between the isolated and polar medium is noted in the final column.

as expected, with the lowest energy associated with terminal Al_{VI}-OH followed by terminal Al_{IV}-OH. Bridge OH bonds have higher dehydroxylation energy than terminal OH bonds for γ -Al₂O₃. The energy of the IIa site is higher than that of the IIb site, because OH is bound to four-coordinate Al, showing that the Al_{IV}-O bond is stronger than the Al_{VI}-O bond. As expected, the highest dehydroxylation energy is obtained for the OH site bound to the three Al_{VI} atoms.

It is interesting to note from the results for AlO(OH) (Table 2) that the bridge OH bond requires less energy to break than the terminal OH bond and significantly lower energy than the corresponding bridge OH bonds of γ -Al₂O₃ (i.e., OH sites IIa and IIb). The lower dehydroxylation energy associated with the OH bridge bond may cause AIH formation throughout the AlO(OH) crystal structure. This energy is similar to that required for bond breaking of the terminal OH groups of γ -Al₂O₃ (i.e., OH sites Ia and Ib, Table 2), but the surface density of the bridged OH sites of AlO(OH) (~ 9.3 OH/nm²) is much higher than the surface OH density of the Ia and Ib sites of γ -Al₂O₃ (~ 2.3 and ~ 0.9 OH/nm²). Thus, the OH

bridge bonds, located throughout the crystal structure of AlO(OH), are likely to be the most active sites for dissolution and AIH formation. Also interesting in Table 2 is the low dehydration energy associated with the two H₂O sites on (100) surface of γ -AlO(OH). The removal of H₂O sites with low dehydration energies may produce a higher pH for the γ -AlO(OH) solution compared with the γ -Al₂O₃ solution.

Table 3 shows the dehydroxylation energies (eq 1b) obtained with the γ -Al₂O₃ cluster models at the B3-LYP/D3/SVP level of theory. A strong influence of the polar environment is found, reducing ΔE_{dhx} considerably in relation to the isolated systems. This reduction reflects the high solvation energy of the separate ions (positively charged surface and hydroxyl anion) and their stabilization in the polar environment compared to the neutral surface. Thus, the aqueous environment plays an important role in the formation of the AIH moiety. The ΔE_{dhx} values are significantly larger in the cluster calculations in comparison to the slab results, which is a consequence of the problem in the calculation of charged systems using periodic models. Nonetheless, the important observation is that the trends in the dehydroxylation energies from the slab and cluster calculations are similar, and the polar environment of the ionic acid solution may weaken the hydroxyl bonding on the order of 40–50%, thereby promoting reactions.

3.2. Powder XRD Analysis. Table 4 shows the PXRD results for the product materials from both precursor powders prepared from the ionic acid solution. Note that the average concentrations and standard deviations are shown as well as data for five separate experiments using the protocol described in this section for each precursor powder. Table 4 shows from the five separate experiments that there are significant variations in AIH formation from both precursor powders, which is also observed in previous work.^{9,10} Overall, the actual yield varied from 11 to 33 wt % AIH for γ -Al₂O₃ and 1 to 11 wt % AIH for γ -AlO(OH) (Table 4). Also, HI₃O₈ is abundant in all samples in Table 4.

If precursor dissolution is the first step toward AIH formation, then the rate for AIH formation from γ -AlO(OH) is slower than from γ -Al₂O₃ inferred from the higher AIH concentrations achieved from γ -Al₂O₃ compared with γ -AlO(OH) shown in Table 4. Slower dissolution rates from γ -AlO(OH) compared with γ -Al₂O₃ can also be inferred from

Table 4. Product Composition When AIH is Formed from γ -Al₂O₃ or γ -AlO(OH) in Iodic Acid, with Crystalline Phase Concentrations Reported as wt %^a

precursor material	PXRD phase					avg. AIH	std. dev.
	AIH	HI ₃ O ₈	others and amorphous	AlO(OH)			
γ -Al ₂ O ₃	11.7	88.3				20.56	10.02
	6.1	46.0	47.9				
	26.0	55.7	18.4				
	26.0	55.6	18.5				
	33.0	60.5	6.5				
γ -AlO(OH)	11.4	79.2		9.4		6.22	3.70
	7.7	83.2	9.1				
	3.8	82.4	13.6				
	7.6	85.8	6.6				
	1.0	88.8	10.6				

^aFive separate experiments for each precursor material were performed to show variability in AIH concentration for the same synthesis protocol. Average AIH concentration and standard deviation are also reported. The molar ratios of γ -Al₂O₃/HIO₃ and γ -AlO(OH)/HIO₃ were 1:6 and 1:10, respectively.

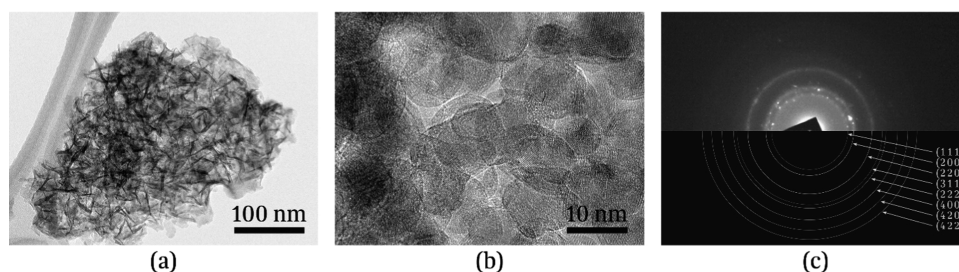


Figure 3. TEM-BF images of the products from γ -AlO(OH)/AIH nanoparticles: (a) unreacted mixture of γ -AlO(OH), (b) a representative region of particles possessing high crystallinity, (c) SAD pattern from (b) and indexed as γ -Al₂O₃.

solution curves reported in refs 31 and 32, respectively. Also, Table 1 shows that there is a ~ 100 m²/g difference in the specific surface area (SSA) between γ -Al₂O₃ and γ -AlO(OH) that may influence the dissolution and AIH formation. Particles with higher SSA (i.e., γ -AlO(OH)) will require more liquid to increase the wetting surface and facilitate dissolution and AIH formation.

The samples containing 11 wt % AIH from both precursor materials were further characterized using TEM and XPS.

3.3. TEM Analysis. The findings from TEM structural and chemical analyses suggest significantly different interactions of the iodic acid solution with γ -AlO(OH) and γ -Al₂O₃ that are linked to hydroxyl bonds and shown in Figures 3–7. Through surveying different regions of γ -AlO(OH)/AIH at lower magnifications, the sample contained residual γ -AlO(OH), as well as γ -Al₂O₃, and iodinated species identified most likely as HI₃O₈. For γ -AlO(OH)/AIH, in almost every region examined, there were numerous, relatively large amounts of a material that was beam sensitive and volatile; we hypothesize that this material is HI₃O₈, because it volatilizes at relatively low temperatures, ~ 200 °C.³⁰ Once these features, which were initially dark and nontransparent, were exposed to the electron beam at higher magnifications for imaging, they bubbled rapidly and then revealed the structure and chemistry of the remaining, freshly exposed crystalline material. Regions of predominantly γ -AlO(OH) were also observed (Figure 3a), indicating the incomplete dissolution of γ -AlO(OH) in iodic acid solution. Figure 3b is a region of predominantly single-crystal nanoparticles. The corresponding SAD pattern matches well with γ -Al₂O₃ (Figure 3c) and indicates that γ -Al₂O₃ is formed from γ -AlO(OH) in the iodic acid solution. It is noted that γ -Al₂O₃ nanoparticles can be formed by the topotactic transformation of AlO(OH) influenced by calcination and dehydration of AlO(OH) according to the reaction^{35,36}



Figures 4 shows the component maps acquired for the γ -AlO(OH)/AIH sample and analyzed by AXSIA using the spatially simple option. Figure 4a is the STEM-BF image, and Figure 4b shows the composite overlay of two contributing components shown in red and green in Figure 4c,d, respectively. The component determined to be the Cu support film is not shown for clarity.

Figure 5 is the overlay of the two XEDS spectra of the components corresponding to Figure 4c,d. The curves in Figure 5a were normalized against Cu-L X-ray line, whereas the green curve in Figure 5b was normalized against O-K X-ray line to show that the Al/O ratio remains constant for both normalizations. The intensities above 3 keV are scaled by a factor of 50 to more clearly show the iodine (I-L) peaks.

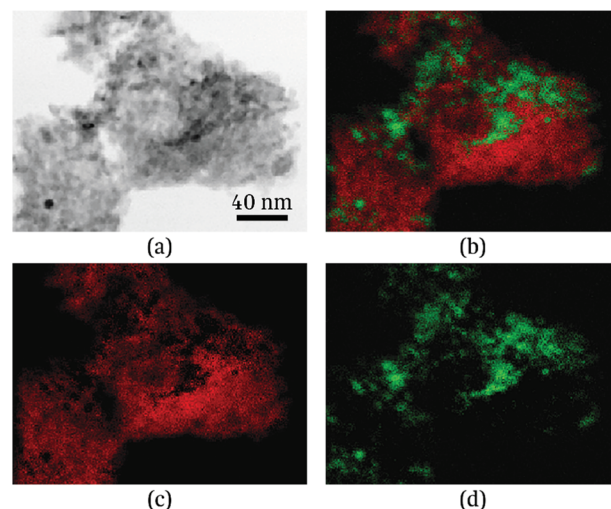


Figure 4. Component phase maps for the AlO(OH)/AIH sample: (a) STEM-BF image of the region analyzed, (b) composite phase overlay, (c) component 1 low-density phase, (d) component 2 high-density phase.

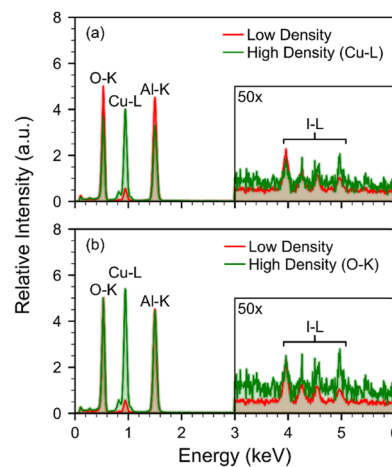


Figure 5. (a) XEDS overlaid component spectra scaled to Cu-L X-ray line and corresponding to Figure 4b, (b) the same XEDS overlaid component spectra rescaled to the O-K X-ray line. The comparison shows that the Al/O ratio remains constant for both normalizations.

Examining the contrast of the STEM-BF image of Figure 4a, one can see clear diffraction contrast coming from areas of the sample designated by the green component phase. The Cu signal is due to X-rays from the sample fluorescing the TEM Cu support grid. With the higher relative intensity of the Cu-L peaks seen in the spectra of Figure 5a, it can be concluded that

the green component phase has a higher density than the red component phase and produces a higher relative Cu signal because of a higher count rate. To compare the relative Al and O concentrations, the two spectra were normalized relative to the O-K peak with the overlay shown in Figure 5b that nearly perfectly overlap. It is apparent that the two-component phases shown in Figure 4c,d have the same Al/O ratio but with different relative Cu-L intensities. For the red component, the iodine peaks have a good signal to background ratio, because iodine is the predominant component with high total counts. When the iodine peaks from the green component are examined in Figure 5b, they exhibit a poorer signal to background ratio, because iodine is the minority component and has fewer counts. However, close inspection shows that the integrated peak intensities relative to an averaged background are essentially the same as the red component phase.

The conclusion from this analysis is that the red and green component phases in Figures 4 and 5 are the same but differ in density. The higher density of the green component phase could be due to some of the particles having a larger relative particle size, which produces the stronger diffraction contrast seen in the STEM-BF image. Table 4 indicates that this sample is 79.2% HI_3O_8 , 9.4% $\text{AlO}(\text{OH})$, and 11.4% AlH ; however, the TEM analysis cannot clearly distinguish these phases. The spectrum in Figure S2 shows the cumulative XEDS from the spectrum image of the area in Figure 4 in TEM mode and shows that the overall iodine concentration is low. Further analysis with XPS presented below provided more detailed species information.

Figure 6 displays the unique surface roughness and highly crystalline spherical particles from the $\gamma\text{-Al}_2\text{O}_3/\text{AlH}$ sample

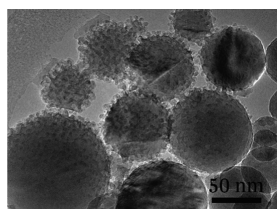


Figure 6. TEM image of freshly synthesized $\gamma\text{-Al}_2\text{O}_3/\text{AlH}$ nanoparticles. The AlH coating is seen as protruding nodules on the particle surface similar to that on nAl .¹⁷

shortly after it was freshly prepared. The rough surface may be comprised of numerous small AlH crystals shown as protruding nodules that are not uniformly coating all of the nanoparticles. Similar extruded nodules of AlH were seen in TEM images of nAl particles with AlH formed on the surface.¹⁰ It is likely that partially dissolved $\gamma\text{-Al}_2\text{O}_3$ recrystallizes with AlH formed on the surface of $\gamma\text{-Al}_2\text{O}_3$ particles, via a mechanism like the Al_2O_3 shell replaced by the AlH coating on nAl particles observed and explained by Smith et al.¹¹

We found that the coating on the $\gamma\text{-Al}_2\text{O}_3$ particles as seen in the Supporting Information Figure S3 had changed over a period of 6 months. As evident in Figure S3a, the originally protruding nodules have partially diminished and become more sparsely decorated around the particles. The XEDS spectrum shown in Figure S3e is acquired from the center of the sample in Figure S3a. It is possible that this morphological change is due to the evaporation of iodine from the sample and

perhaps redeposition. During exposure to the beam in the TEM, iodine was seen to be volatile. Comparing images and XEDS spectra taken before and after a few minutes of exposure to the electron beam shows that the iodine-rich phase on and around $\gamma\text{-Al}_2\text{O}_3$ particles disappears. Figure S3e shows the overlaid XEDS spectra before (red) and after (blue) exposure and clearly shows that the iodine becomes nondetectable after this relatively short exposure. The disappearance of the iodine-rich phase may be an indication of the molecular species present in the sample. We have previously shown that AlH volatilizes at low temperatures ($\sim 140\text{ }^\circ\text{C}$)¹⁰ such that the iodine disappearance (and volatilization) upon beam exposure is consistent with the thermal behavior of AlH . However, HI_3O_8 also has a low dehydration temperature of $\sim 200\text{ }^\circ\text{C}$ such that iodine volatilization may also come from HI_3O_8 .³⁰ However, when HIO_3 dissociates, iodine does not volatilize but transforms into condensed phase HI_3O_8 and H_2O vapor ($\sim 100\text{ }^\circ\text{C}$).³⁷ Therefore, the volatilization of iodine is most likely associated with AlH or HI_3O_8 dissociation because of their low dehydration temperatures.

Figure 7 shows the component phase maps acquired with the STEM-BF image (Figure 7a) for the $\gamma\text{-Al}_2\text{O}_3/\text{AlH}$ sample and postprocessed by AXSIA. Figure 7b shows the composite overlay of the detected phases with the corresponding individual component maps shown in Figure 7c,d, for the $\gamma\text{-Al}_2\text{O}_3$ and AlH phases, respectively, and the carbon support film shown in Figure 7e.

Figure 8 shows the corresponding overlaid component XEDS spectra of Figure 7b. As evident in the overlay image (Figure 7b) and AlH component map (Figure 7d), AlH is formed on the surface of $\gamma\text{-Al}_2\text{O}_3$ particles. The lower Al-K to O-K ratio for AlH relative to that for an Al_2O_3 phase is consistent with this identification. To determine whether the iodine-rich phase on the surface of the particles is HI_3O_8 or AlH , XPS analysis was further performed and presented below.

3.4. XPS Analysis. The XPS analysis was performed to identify surface species by measuring binding energies. The XPS general survey scans for $\gamma\text{-Al}_2\text{O}_3/\text{AlH}$ and $\gamma\text{-AlO}(\text{OH})/\text{AlH}$ and their corresponding atomic concentration AC % of all strong photopeaks are detailed in Tables S2, S3 and Figures S4–S9, but the atomic concentration percentage (AC %) from XPS analysis of O 1s peaks is shown in Table 5. Results in Table 5 confirm that OH^- and absorbed H_2O are initially higher in $\gamma\text{-AlO}(\text{OH})$ than $\gamma\text{-Al}_2\text{O}_3$ (i.e., 38.54 and 19.72 compared with 35.73 and 4.52, respectively). More hydration is measured for $\gamma\text{-AlO}(\text{OH})$ and consistent with a higher surface density of OH in $\gamma\text{-AlO}(\text{OH})$ than $\gamma\text{-Al}_2\text{O}_3$. Upon the formation of AlH , OH^- concentration is reduced by 61% from $\gamma\text{-AlO}(\text{OH})$ but only 13% from $\gamma\text{-Al}_2\text{O}_3$, Table 5. The observed reduced OH^- concentration after the synthesis of AlH suggests that the consumption of OH^- species plays a vital role in the formation of AlH , as predicted in the DFT calculations (Tables 2 and 3).

The atomic concentration percentage (AC %) from XPS analysis of I $3d_{5/2}$ peaks is shown in Table 6. The iodate (IO_3^-) peaks are at a distinctly different binding energy (625–626 eV) compared with HIO_3 (623.1 eV), HI_3O_8 (623.2 eV), and I_2O_5 (623.3 eV). The identification of IO_3^- correlates with AlH that has a crystallographic structure shown in Figure 9.³⁸ The IO_3^- species bond with the aluminum hexahydrate $[\text{Al}(\text{H}_2\text{O})_6]^{3+}$ to balance the charge and form AlH $[\text{Al}(\text{IO}_3)_3(\text{HIO}_3)_2 \cdot 6\text{H}_2\text{O}]$. The XPS data in Table 6 reveal 21 AC % AlH from $\gamma\text{-Al}_2\text{O}_3/\text{AlH}$ and 36 AC % AlH from $\gamma\text{-$

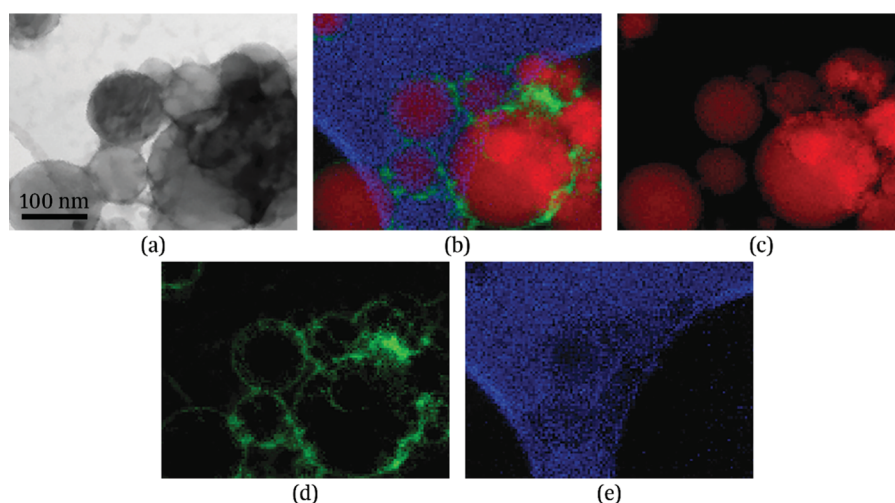


Figure 7. Component phase maps for the γ -Al₂O₃/AIH sample: (a) STEM-BF image of the region acquired analysis, (b) phase overlay, (c) Al₂O₃ phase, (d) AIH phase, (e) carbon phase.

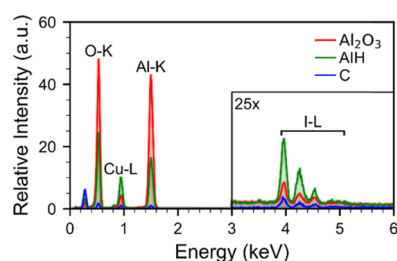


Figure 8. XEDS spectrum corresponding to Figure 7b.

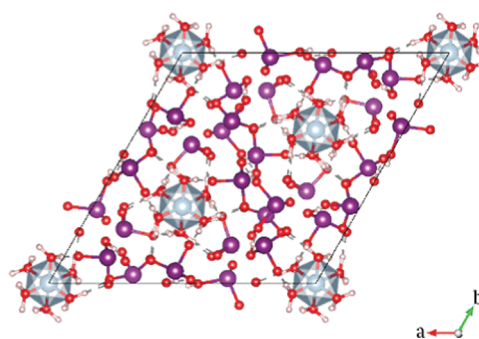


Figure 9. Graphical representation of aluminum iodate hexahydrate (AIH) crystal structure.³⁸ Gray spheres represent Al, red spheres represent O, white spheres represent H, and purple spheres represent I. Note that the Al³⁺ ion is surrounded by six water molecules that are electrostatically bonded to iodates (IO₃⁻) to form Al(IO₃)₃(HIO₃)₂·6H₂O.

Table 5. Atomic Concentration Percentages (AC %) of XPS O 1s Spectra from Precursor Materials and Solid Product Materials after AIH Formation in Iodic Acid Solution (Identified as γ -Al₂O₃/AIH and γ -AlO(OH)/AIH)^a

materials	O ²⁻ (531 eV)	OH ⁻ (532 eV)	absorbed H ₂ O (533–534 eV)
γ -Al ₂ O ₃	59.75	35.73	4.52
γ -Al ₂ O ₃ /AIH	63.31	31.12	5.57
γ -AlO(OH)	41.74	38.54	19.72
γ -AlO(OH)/AIH	73.75	14.99	11.27

^aBinding energy is noted in parentheses.

Table 6. Atomic Concentration Percentages (AC %) Measured with XPS I 3d_{5/2} Spectra from Solid Product Materials after AIH Formation in Iodic Acid Solution (Identified as γ -Al₂O₃/AIH and γ -AlO(OH)/AIH)^a

materials	HI ₃ O ₈ (623.2 eV)	I ₂ O ₅ (623.3 eV)	IO ₃ ⁻ (625–626 eV)
γ -Al ₂ O ₃ /AIH	73.68	4.80	21.52
γ -AlO(OH)/AIH	58.28		36.42

^aBinding energy is noted in parentheses.

AlO(OH)/AIH. All XPS data identify surface chemistry with a penetration depth of about 5 nm into the sample surface. Also, the TEM results shown in Figure 7b indicate that AIH from γ -Al₂O₃/AIH is identified as the surface (~5–10 nm) coating larger (~50 nm) particles. The TEM results shown in Figure 4 cannot distinguish AIH from γ -AlO(OH)/AIH. The identification of AIH via IO₃⁻ peaks (Table 6) coupled with the removal of –OH bonds shown in Table 5 is consistent with

DFT calculations showing that hydroxyl bonds associated with γ -Al₂O₃ and γ -AlO(OH) are reactive sites for dissolution and subsequent formation of AIH.

4. CONCLUSIONS

Density functional theory calculations show that the dehydroxylation energy of bridge OH bonds throughout the γ -AlO(OH) structure is nearly equivalent to the terminal OH bonds on the γ -Al₂O₃ particle surface, such that these are reactive sites for dissolution and subsequent formation of aluminum iodate hexahydrate (AIH). The DFT calculations are experimentally supported by the observation that AIH formation is favored on the surface of γ -Al₂O₃ particles attributed to the lower dehydroxylation energies of the many terminal –OH bonds on the surface. Also, dehydroxylation energies from cluster calculations using a polar environment show that the iodic acid solution may weaken hydroxyl bonding on the order of 40–50%, thereby promoting surface reactions. These predictions are confirmed experimentally via surface chemistry analysis using TEM and XPS.

Experimentally, the AIH yield from γ -Al₂O₃ is higher (up to 33%) than from γ -AlO(OH) (up to 11%). If dissolution is the first step in AIH formation, the dissolution rate for γ -Al₂O₃ is higher than γ -AlO(OH) because for the same time in the

solution, more AIH is formed from γ -Al₂O₃ than from γ -AlO(OH). The XPS results show that hydroxyl species are removed from γ -AlO(OH) and γ -Al₂O₃ prior to AIH formation, consistent with DFT predictions that hydroxyl groups are reactive sites. The TEM data indicate dramatically different surface morphologies between the two products. From γ -AlO(OH), iodinated species appear to be located throughout the particle mixture, whereas from γ -Al₂O₃, AIH is located on the surface of particles. The coupled calculations and experimental results indicate that AIH formation is facilitated by the hydration layer on the surface of γ -Al₂O₃.

■ ASSOCIATED CONTENT

● Supporting Information

The Supporting Information is available free of charge on the ACS Publications website at DOI: 10.1021/acs.jpcc.9b02663.

Stoichiometry and lateral vectors of the computational unit cells of the periodic slab models of γ -Al₂O₃ and AlO(OH) used in the VASP calculations; characterization of starting Al₂O₃ and AlO(OH) materials via XRD and TEM; X-ray elemental diffraction spectra (XEDS) from AlO(OH)/AIH and Al₂O₃/AIH; XPS data analysis from AlO(OH)/AIH and Al₂O₃/AIH (PDF)

■ AUTHOR INFORMATION

Corresponding Authors

*E-mail: Chi-chin.wu.civ@mail.mil. Tel.: +1-410-306-1905 (C.-C.W.).

*E-mail: adelia.aquino@ttu.edu. Tel.: +1-806-789-1348 (A.J.A.A.).

*E-mail: daniel.tunega@univie.ac.at. Tel.: +43-1-47654-91148 (D.T.).

*E-mail: michelle.pantoya@ttu.edu. Tel.: +1-806-834-3733 (M.L.P.).

ORCID

Adelia J. A. Aquino: 0000-0003-4891-6512

Michelle L. Pantoya: 0000-0003-0299-1832

Notes

The authors declare no competing financial interest.

■ ACKNOWLEDGMENTS

The authors are grateful for support from the Army Research Office under award W911NF-17-1-0387 and our Program Manager, Dr Ralph Anthenien. A.J.A.A. and D.T. are thankful for computer time at the Vienna Scientific Cluster (VSC), Project No. 70544. The collaboration between the US Army Research Laboratory and Texas Tech University is partially supported by the ARL Director's Research Award (DIRA) under the External Collaboration Initiative (ECI) DEC18-WM-009. We are also thankful to Dr Juliusz Warzywoda and Dr Daniel Unruh from the Whitacre College of Engineering and Chemistry Department at TTU, respectively, for the analysis of their materials. We are thankful for helpful discussions with Kelsea Miller and Dr Dylan Smith.

■ REFERENCES

- (1) Levitas, V. I.; Asay, B. W.; Son, S. F.; Pantoya, M. Melt Dispersion Mechanism for Fast Reaction of Nanothermites. *Appl. Phys. Lett.* **2006**, *89*, No. 071909.
- (2) Levitas, V. I.; Asay, B. W.; Son, S. F.; Pantoya, M. Mechanochemical Mechanism for Fast Reaction of Metastable

Intermolecular Composites Based on Dispersion of Liquid Metal. *J. Appl. Phys.* **2007**, *101*, No. 083524.

- (3) Pantoya, M.; Levitas, V.; Granier, J.; Henderson, J. The Effect of Bulk Density on the Reaction Dynamics in Nano and Micron Particulate Thermites. *J. Propul. Power* **2009**, *25*, 465–470.

- (4) Jouet, R. J.; Warren, A. D.; Rosenberg, D. M.; Bellitto, V. J.; Park, K.; Zachariah, M. R. Surface Passivation of Bare Aluminum Nanoparticles Using Perfluoroalkyl Carboxylic Acids. *Chem. Mater.* **2005**, *17*, 2987–2996.

- (5) Foley, T. J.; Johnson, C. E.; Higa, K. T. Inhibition of Oxide Formation on Aluminum Nanoparticles by Transition Metal Coating. *Chem. Mater.* **2005**, *17*, 4086–4091.

- (6) Crouse, C.; Shin, E.; Murray, P.; Spowart, J. Solution Assisted Laser Ablation Synthesis of Discrete Aluminum Nanoparticles. *Mater. Lett.* **2010**, *64*, 271–274.

- (7) Crouse, C. A.; Pierce, C. J.; Spowart, J. E. Influencing Solvent Miscibility and Aqueous Stability of Aluminum Nanoparticles through Surface Functionalization with Acrylic Monomers. *ACS Appl. Mater. Interfaces* **2010**, *2*, 2560–2569.

- (8) Lewis, W. K.; Rumchik, C.; Smith, M.; Fernando, K. S.; Crouse, C. A.; Spowart, J. E.; Gulians, E. A.; Bunker, C. E. Comparison of Post-Detonation Combustion in Explosives Incorporating Aluminum Nanoparticles: Influence of the Passivation Layer. *J. Appl. Phys.* **2013**, *113*, No. 044907.

- (9) Smith, D. K.; Bello, M. N.; Unruh, D. K.; Pantoya, M. L. Synthesis and Reactive Characterization of Aluminum Iodate Hexahydrate Crystals [Al(H₂O)₆](IO₃)₃(HIO₃)₂. *Combust. Flame* **2017**, *179*, 154–156.

- (10) Gottfried, J. L.; Smith, D. K.; Wu, C.-C.; Pantoya, M. L. Improving the Explosive Performance of Aluminum Nanoparticles with Aluminum Iodate Hexahydrate (AIH). *Sci. Rep.* **2018**, *8*, No. 8036.

- (11) Smith, D. K.; Unruh, D. K.; Wu, C.-C.; Pantoya, M. L. Replacing the Al₂O₃ Shell on Al Particles with an Oxidizing Salt, Aluminum Iodate Hexahydrate. Part I: Reactivity. *J. Phys. Chem. C* **2017**, *121*, 23184–23191.

- (12) Smith, D. K.; Unruh, D. K.; Pantoya, M. L. Replacing the Al₂O₃ Shell on Al Particles with an Oxidizing Salt, Aluminum Iodate Hexahydrate. Part II: Synthesis. *J. Phys. Chem. C* **2017**, *121*, 23192–23199.

- (13) Cradwick, P. D.; de Endredy, A. S. Crystal Structure of Aluminium Iodate–Hydrogen Iodate–Water (1/1/6) and Preparation of Anhydrous Aluminium Iodate. *J. Chem. Soc., Dalton Trans.* **1977**, *2*, 146–149.

- (14) Kidyarov, B. Growth of Polar Al(IO₃)₃·8H₂O Crystals from Aqueous Solutions. *Bull. Russ. Acad. Sci.: Phys.* **2010**, *74*, 1255–1256.

- (15) Kresse, G.; Furthmüller, J. Efficient Iterative Schemes for Ab Initio Total-Energy Calculations Using a Plane-Wave Basis Set. *Phys. Rev. B: Condens. Matter Mater. Phys.* **1996**, *54*, 11169.

- (16) Kresse, G.; Hafner, J. Ab Initio Molecular Dynamics for Open-Shell Transition Metals. *Phys. Rev. B: Condens. Matter Mater. Phys.* **1993**, *48*, 13115.

- (17) Perdew, J. P.; Burke, K.; Wang, Y. Ab Initio Molecular Dynamics for Open-Shell Transition Metals. *Phys. Rev. B: Condens. Matter Mater. Phys.* **1996**, *54*, 16533.

- (18) Kresse, G.; Joubert, D. From Ultrasoft Pseudopotentials to the Projector Augmented-Wave Method. *Phys. Rev. B: Condens. Matter Mater. Phys.* **1999**, *59*, 1758.

- (19) Blöchl, P. E. Projector Augmented-Wave Method. *Phys. Rev. B: Condens. Matter Mater. Phys.* **1994**, *50*, 17953.

- (20) Grimme, S.; Antony, J.; Ehrlich, S.; Krieg, H. A Consistent and Accurate Ab Initio Parametrization of Density Functional Dispersion Correction (Dft-D) for the 94 Elements H–Pu. *J. Chem. Phys.* **2010**, *132*, No. 154104.

- (21) Becke, A. D. Density-Functional Thermochemistry. III. The Role of Exact Exchange. *J. Chem. Phys.* **1993**, *98*, 5648–5652.

- (22) Schäfer, A.; Horn, H.; Ahlrichs, R. Fully Optimized Contracted Gaussian Basis Sets for Atoms Li to Kr. *J. Chem. Phys.* **1992**, *97*, 2571–2577.

- (23) Ahlrichs, R.; Bär, M.; Häser, M.; Horn, H.; Kölmel, C. Electronic Structure Calculations on Workstation Computers: The Program System Turbomole. *Chem. Phys. Lett.* **1989**, *162*, 165–169.
- (24) Klamt, A.; Schüürmann, G. Cosmo: A New Approach to Dielectric Screening in Solvents with Explicit Expressions for the Screening Energy and Its Gradient. *J. Chem. Soc., Perkin Trans. 2* **1993**, *5*, 799–805.
- (25) Smrčok, L.; Langer, V.; Křest'an, J. γ -Alumina: A Single-Crystal X-Ray Diffraction Study. *Acta Crystallogr., Sect. C: Cryst. Struct. Commun.* **2006**, *62*, i83–i84.
- (26) Knözinger, H.; Ratnasamy, P. Catalytic Aluminas: Surface Models and Characterization of Surface Sites. *Catal. Rev.: Sci. Eng.* **1978**, *17*, 31–70.
- (27) Padhye, R.; Aquino, A. J.; Tunega, D.; Pantoya, M. L. Effect of Polar Environments on the Aluminum Oxide Shell Surrounding Aluminum Particles: Simulations of Surface Hydroxyl Bonding and Charge. *ACS Appl. Mater. Interfaces* **2016**, *8*, 13926–13933.
- (28) Noel, Y.; Demichelis, R.; Pascale, F.; Ugliengo, P.; Orlando, R.; Dovesi, R. Ab Initio Quantum Mechanical Study of γ -AlOOH Boehmite: Structure and Vibrational Spectrum. *Phys. Chem. Miner.* **2009**, *36*, 47–59.
- (29) Prange, M. P.; Zhang, X.; Bowden, M. E.; Shen, Z.; Ilton, E. S.; Kerisit, S. N. Predicting Surface Energies and Particle Morphologies of Boehmite (γ -AlOOH) from Density Functional Theory. *J. Phys. Chem. C* **2018**, *122*, 10400–10412.
- (30) Little, B. K.; Emery, S. B.; Nittinger, J. C.; Fantasia, R. C.; Lindsay, C. M. Physiochemical Characterization of Iodine (V) Oxide, Part 1: Hydration Rates. *Propellants, Explos., Pyrotech.* **2015**, *40*, 595–603.
- (31) Bénézeth, P.; Palmer, D. A.; Wesolowski, D. J. Dissolution/Precipitation Kinetics of Boehmite and Gibbsite: Application of a Ph-Relaxation Technique to Study near-Equilibrium Rates. *Geochim. Cosmochim. Acta* **2008**, *72*, 2429–2453.
- (32) Carrier, X.; Marceau, E.; Lambert, J.-F.; Che, M. Transformations of γ -Alumina in Aqueous Suspensions: I. Alumina Chemical Weathering Studied as a Function of Ph. *J. Colloid Interface Sci.* **2007**, *308*, 429–437.
- (33) Keenan, M. R.; Kotula, P. G. Accounting for Poisson Noise in the Multivariate Analysis of ToF-Sims Spectrum Images. *Surf. Interface Anal.* **2004**, *36*, 203–212.
- (34) Kotula, P. G.; Keenan, M. R.; Michael, J. R. Automated Analysis of Sem X-Ray Spectral Images: A Powerful New Microanalysis Tool. *Microsc. Microanal.* **2003**, *9*, 1–17.
- (35) Krokidis, X.; Raybaud, P.; Gobichon, A.-E.; Rebours, B.; Euzen, P.; Toulhoat, H. Theoretical Study of the Dehydration Process of Boehmite to γ -Alumina. *J. Phys. Chem. B* **2001**, *105*, 5121–5130.
- (36) Ren, T.-Z.; Yuan, Z.-Y.; Su, B.-L. Microwave-Assisted Preparation of Hierarchical Mesoporous–Macroporous Boehmite Aloh and γ -Al₂O₃. *Langmuir* **2004**, *20*, 1531–1534.
- (37) Smith, D. K.; McCollum, J.; Pantoya, M. L. Effect of Environment on Iodine Oxidation State and Reactivity with Aluminum. *Phys. Chem. Chem. Phys.* **2016**, *18*, 11243–11250.
- (38) Kuppers, H.; Schafer, W.; Will, G. X-ray and Neutron-Diffraction Study of Al(IO₃)₃·2HIO₃·6H₂O. *Z. Kristallogr.* **1982**, *159*, 231–238.